



Investigation of the Lithiation and Delithiation Conversion Mechanisms of Bismuth Fluoride Nanocomposites

M. Bervas,^{a,b} A. N. Mansour,^{c,*} W.-S. Yoon,^{d,*} J. F. Al-Sharab,^b F. Badway,^{a,b}
F. Cosandey,^b L. C. Klein,^b and G. G. Amatucci^{a,b,*z}

^aEnergy Storage Research Group, and ^bDepartment of Materials Science and Engineering, Rutgers, The State University of New Jersey, Piscataway, New Jersey 08854, USA

^cNaval Surface Warfare Center, Carderock Division, West Bethesda, Maryland 20817-5700, USA

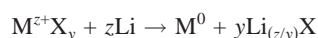
^dBrookhaven National Laboratory, Upton, New York 11973, USA

Combined in situ X-ray diffraction, in situ X-ray absorption spectroscopy, and selected area electron diffraction analyses have confirmed the occurrence of a reversible conversion reaction in the BiF₃/C nanocomposite upon cycling, which leads to the formation of Bi⁰ and LiF during lithiation and the reformation of BiF₃ during delithiation. It has been shown that only the high-pressure tysonite phase of BiF₃ reforms during the oxidation sweep and that no bismuth fluoride compound with an oxidation state of the bismuth lower than 3 is formed as intermediate during the lithiation or delithiation reactions. Finally, it has been demonstrated that the different plateaus or pseudo plateaus observed on the lithiation and delithiation voltage profiles stem from polarization changes brought about by the dramatic structural changes occurring in the nanocomposite upon cycling. A model, based on the variation of the electronic and ionic transport mechanisms as a function of the state of completion of the conversion and reconversion reactions, is proposed to explain those polarization changes.

© 2006 The Electrochemical Society. [DOI: 10.1149/1.2167951] All rights reserved.

Manuscript submitted June 8, 2005; revised manuscript received October 3, 2005. Available electronically March 2, 2006.

Conversion reactions are lithiation reactions in which the active material is fully reduced by lithium to the metal according to the following equation



where M stands for a cation and X an anion. As all the oxidation states of the material are utilized, capacities much higher than in the intercalation reactions currently used in rechargeable Li-ion batteries can in theory be obtained, thereby leading to much higher energy densities.

Conversion reactions have been known for a long time in primary battery applications with, for instance, the Li/CuO and Li/CF_x systems that are still utilized today.¹ Due to the highly destructive nature of the reaction, which literally involves the breaking of chemical bonds and the formation of new ones, it has long been thought that such reactions were irreversible. To the best of our knowledge, Besenhard was the first to report the electrochemical reversibility of a conversion reaction in 1978² in a paper on bismuth chalcogenides. In this paper, it was shown that Bi₂S₃ was reduced into Bi⁰ and Li₂S during lithiation and was reoxidized with 75% efficiency during the following delithiation; but this reversibility was observed for one cycle only. Selwyn et al. reported in 1987 that the conversion reactions occurring in Mo and W dichalcogenides exhibited some electrochemical reversibility but did not clearly identify the compound(s) formed during the delithiation.³ The possibility to have full electrochemical and structural reversibility in conversion reactions of dichalcogenides during charge has been proven for the first time only about 5 years ago by Tarascon's group.⁴ They reported specific capacities as high as 700 mAh/g and full reversibility for several tenth of cycles when different transition metal oxides⁴ and sulfides⁵ were used as negative electrode or low-voltage positive electrodes.

As the output voltage of a conversion reaction scales with the ionicity of the M–X bond, metal nitride,^{6,7} sulfides,^{2,5} and oxide^{4,8} have low output voltage ranging from about 0.5 to about 1 V. These low voltages make these compounds attractive for application as active materials at the anode side of the lithium battery. Only in metal halides is the ionicity of the M–X bond sufficient to have a conversion reaction output voltage high enough for positive elec-

trode applications. Metal chlorides are not a practical solution because they dissolve in the electrolyte and are heavy, leaving metal fluorides as the only possible choice.

Metal fluorides are electronic insulators and cannot be used as conventional electrode materials. Only the lower voltage metal fluorides have been shown to have any appreciable reversible reactivity in the macrostructured state.⁹ We have demonstrated that the electrochemical activity of high-voltage/high-energy-density metal fluorides can truly be enabled when prepared in a nanostructured state and dispersed in a conductive matrix such as carbon or metal oxide.^{10,11} In carbon metal fluoride nanocomposites (CMFNCs) the carbon matrix insures a high electronic conductivity while the metal fluoride nanoparticles bring short diffusion pathways for the lithium and the possibility of electron tunneling. With this approach, specific capacities as high as 600 mAh/g could be extracted from the FeF₃/C nanocomposite at slightly elevated temperature with full reversibility for several tens of cycles.¹² Our group also recently showed that in metal oxyfluorides the fluorine component was converting first during lithiation on a high-voltage plateau, followed by the oxide component on a conversion plateau below 2 V. Therefore, metal oxyfluorides could in theory also be used for cathode application if they are cycled on the high-voltage fluorine conversion plateau.¹³

We have recently reported that the BiF₃ CMFNC exhibits some interesting properties for applications as a positive electrode active material in rechargeable lithium batteries.¹⁴ The conversion reaction that takes place on a 3-V plateau in the bismuth fluoride during lithiation leads to a specific capacity of about 230 mAh/(g of CMFNC), corresponding to a high volumetric energy density of about 5500 Wh/(L of BiF₃). Unlike other CMFNCs, for instance the FeF₃ CMFNC,¹² the BiF₃ CMFNC also displayed an excellent rate capability. Hence, we demonstrated that the utilization of the active material was close to 90% of the theoretical value at a C rate and 65% of the theoretical value at a 4 C rate.¹⁴ This second paper on the BiF₃ CMFNC focuses on the conversion and reconversion reaction mechanisms. It relates the results of a more in-depth study, conducted with combined in situ X-ray diffraction, in situ X-ray absorption, and electron diffraction, on the evolutions of the structure and the microstructure of the active material upon cycling.

Experimental

The tysonite BiF₃/C nanocomposite, denoted *t*-BiF₃ thereafter, has been prepared by high-energy milling for 1 h in a Spex 8000

* Electrochemical Society Active Member.

^z E-mail: gamatucci@rci.rutgers.edu

Report Documentation Page				Form Approved OMB No. 0704-0188	
Public reporting burden for the collection of information is estimated to average 1 hour per response, including the time for reviewing instructions, searching existing data sources, gathering and maintaining the data needed, and completing and reviewing the collection of information. Send comments regarding this burden estimate or any other aspect of this collection of information, including suggestions for reducing this burden, to Washington Headquarters Services, Directorate for Information Operations and Reports, 1215 Jefferson Davis Highway, Suite 1204, Arlington VA 22202-4302. Respondents should be aware that notwithstanding any other provision of law, no person shall be subject to a penalty for failing to comply with a collection of information if it does not display a currently valid OMB control number.					
1. REPORT DATE 03 OCT 2005		2. REPORT TYPE		3. DATES COVERED 00-00-2005 to 00-00-2005	
4. TITLE AND SUBTITLE Investigation of the Lithiation and Delithiation Conversion Mechanisms of Bismuth Fluoride Nanocomposites				5a. CONTRACT NUMBER	
				5b. GRANT NUMBER	
				5c. PROGRAM ELEMENT NUMBER	
6. AUTHOR(S)				5d. PROJECT NUMBER	
				5e. TASK NUMBER	
				5f. WORK UNIT NUMBER	
7. PERFORMING ORGANIZATION NAME(S) AND ADDRESS(ES) Naval Surface Warfare Center,Carderock Division,West Bethesda,MD,20817-5700				8. PERFORMING ORGANIZATION REPORT NUMBER	
9. SPONSORING/MONITORING AGENCY NAME(S) AND ADDRESS(ES)				10. SPONSOR/MONITOR'S ACRONYM(S)	
				11. SPONSOR/MONITOR'S REPORT NUMBER(S)	
12. DISTRIBUTION/AVAILABILITY STATEMENT Approved for public release; distribution unlimited					
13. SUPPLEMENTARY NOTES					
14. ABSTRACT					
15. SUBJECT TERMS					
16. SECURITY CLASSIFICATION OF:			17. LIMITATION OF ABSTRACT Same as Report (SAR)	18. NUMBER OF PAGES 10	19a. NAME OF RESPONSIBLE PERSON
a. REPORT unclassified	b. ABSTRACT unclassified	c. THIS PAGE unclassified			

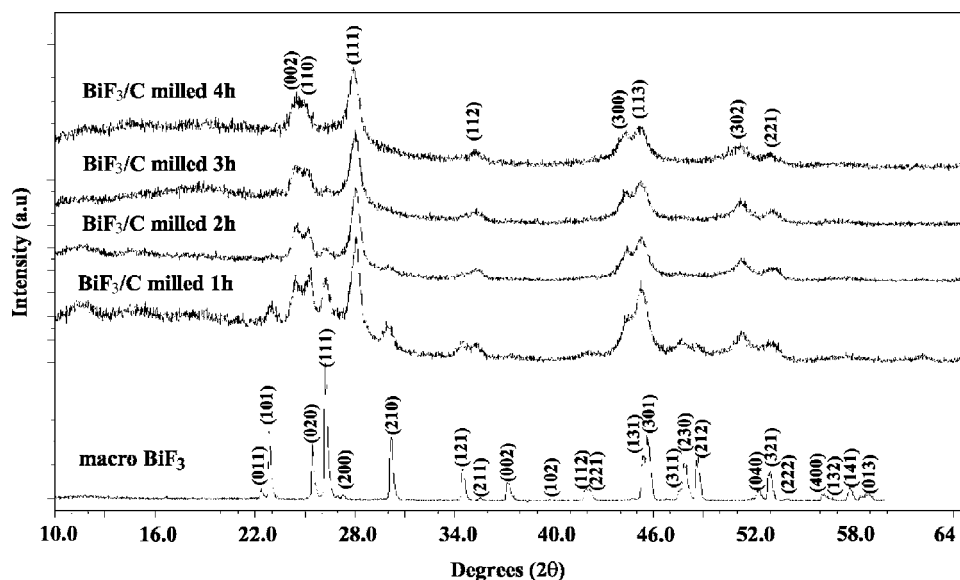


Figure 1. XRD patterns of the pristine macro-BiF₃ and of the macro-BiF₃ high-energy milled in He for 1, 2, 3, and 4 h in the presence of carbon Super P, showing the phase transformation from orthorhombic (SG *Pnma*) to tysonite [SG *P(3)c1*].

mill 85 wt % of BiF₃ (Alfa Aesar) with 15 wt % carbon black (Super P, MMM). The high-energy milling cell and balls were in hardened steel. The high-energy milling cell was sealed and reopened after milling inside an He-filled glove box at -80°C dew point, thus preventing the powder from moisture or oxygen contamination. The orthorhombic BiF₃/C nanocomposite, denoted *o*-BiF₃ thereafter, has been prepared by treating the *t*-BiF₃ nanocomposite with 48% concentrated hydrofluoric acid in a Teflon container. The powder obtained was placed overnight in an oven at 95°C to let the HF evaporate and dried a second time overnight at 120°C under vacuum before entering the glove box. Results previously presented by our group indicated that the tysonite to orthorhombic phase transformation occurs via a dissolution/precipitation mechanism.¹⁴

X-ray diffraction (XRD) analyses were performed on a Scintag X2 using Cu K α radiation. Samples to be analyzed *ex situ* were placed on glass slides and covered with a Kapton film sealed with silicon-based vacuum grease inside the glove box to minimize air exposure. For the *in situ* XRD the electrode was placed in an *in situ* cell prepared by our group. A Beryllium window and an isolation film of Kapton were placed on top of the working electrode to isolate it and the electrolyte from the atmosphere while allowing the X-ray to penetrate. A detailed description of this *in situ* XRD cell will be provided in an upcoming paper.

The transmission electron microscope (TEM) was a Topcon 002B. The powders were first dispersed in anhydrous dimethyl carbonate (DMC), a few drops of which were then disposed on a lacey carbon grid and allowed to dry overnight inside the glove box. The grids were then placed in bags sealed inside the glove box that were reopened at the last moment, thereby minimizing the exposure time to the atmosphere to a few seconds. In order to avoid the decomposition of the material, which occurs relatively quickly under the electron-beam, the samples were scanned in diffraction mode at low brightness until sharp rings appeared and the exposure time to collect the images was kept under 15 s. The selected area electron diffraction (SAED) patterns were interpreted using Process Diffraction software.¹⁵

For the *in situ* X-ray absorption spectroscopy (XAS) experiments, the electron storage ring operated at energy of 2.8 GeV and a current in the range of 150–300 mA. Spectra of the Bi L₃-edge (13,419 eV) were collected in the transmission mode at room temperature with energy intervals per step of 5 eV for the pre-edge region (13,119–13,489 eV) and 0.5 eV for the edge region (13,469–13,489 eV). A *k*-space interval of 0.05 \AA^{-1} was used for the extended X-ray absorption fine structure (EXAFS) region (13,469–14,168 eV). Integration intervals per point were set to 1 s

for all regions. A delay time of 0.3 s was used between successive data points in order for the monochromator to equilibrate at each point. The X-ray absorption fine structure (XAFS) analysis area was set to $10^{-2} \times 10^{-3} \text{ m}^2$. The zero of energy for the photoelectron was taken at the inflection point of the absorption edge. The spectra were normalized to a per atom basis using the average of the absorption cross section over the energy range of 100–400 eV above the edge energy. The EXAFS spectrum, $\chi(k)$, was extracted by fitting a cubic spline procedure to the EXAFS region, which minimized the amplitude of nonphysical peaks in the 0–1 \AA region of the Fourier transforms. Fourier transforms were generated from *k*³-weighted EXAFS spectra (*k*-range 2.45–10.0 \AA^{-1} and a Hanning window of 20%). The data analysis was carried out using the WinXAS software package (ver. 2.3).^{16,17} A detailed description of the *in situ* cell has been provided elsewhere.¹⁸

To prepare the electrodes an acetone-based slurry containing the active material, a poly(vinylidene fluoride-*co*-hexafluoropropylene) (Kynar 2801, Elf Atochem) binder, carbon black (Super P, 3 M), and dibutyl phthalate (Aldrich) plasticizer in the ratio 39:21:8:32 was first prepared. The slurry was then tape casted. Once dried, the tape was placed in 99.8% anhydrous ether (Aldrich) to extract the DBP. After DBP extraction the active material loading of the tape was $57 \pm 1\%$. Disks of about 1 cm² punched from these tapes were tested in coin cell against lithium metal (Johnson Matthey). The coin cells were cycled under controlled temperatures. The batteries were cycled either on an Arbin, a Maccor, or a MacPile (Biologic). Three different electrolytes were used: LiPF₆ salt in a mixture of ethylene carbonate (EC)/propylene carbonate (PC)/diethyl carbonate (DEC)/DMC solvents at 1 M, LiPF₆ in EC/DMC at 1 M, or LiClO₄ in EC/DMC at 0.4 M.

Results and Discussion

Physical characterization.—The XRD patterns of the pristine macro BiF₃ powder and of the macro BiF₃ powder high-energy milled in He in the presence of 15 wt % of carbon Super P for 1 h, 2 h, 3 h, and 4 h are shown on Fig. 1. It is readily apparent from this figure that BiF₃ undergoes a phase transformation from the initial orthorhombic phase (*o*-BiF₃) to a hexagonal tysonite phase (*t*-BiF₃). The calculated lattice parameters of this phase are $a = 7.100 \pm 0.004 \text{ \AA}$ and $c = 7.292 \pm 0.007 \text{ \AA}$. This tysonite phase could be a bismuth oxyfluoride BiO_δF_{3–2δ} where δ can be as low as 0.01 or the high-pressure form of BiF₃, which are isostructural and have almost identical lattice parameters.^{19,20} It has been shown by Ardashnikova et al. that the pure fluoride BiF₃ should retransform to

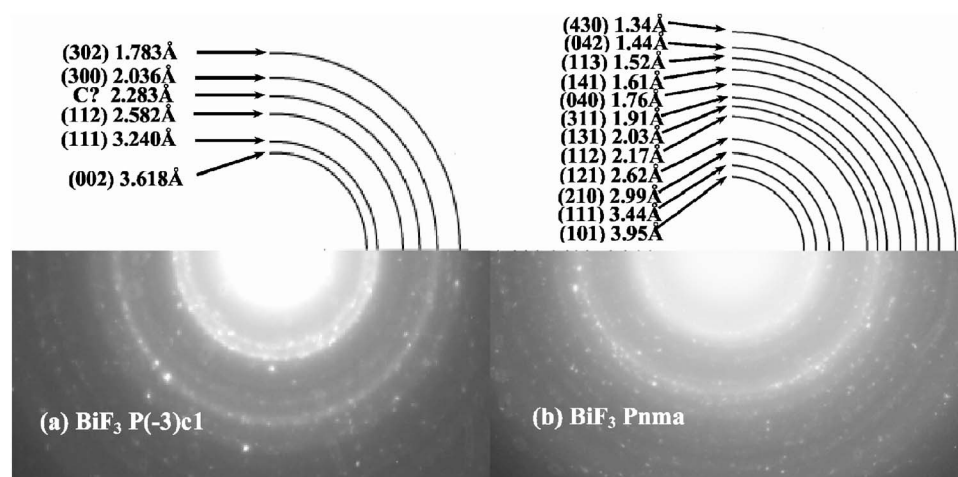


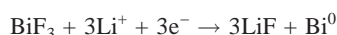
Figure 2. SAED on the BiF_3/C nanocomposite high-energy milled for 1 h, characteristic of (a) the pure tysonite or (b) the pure orthorhombic phases.

the orthorhombic BiF_3 upon annealing to 350°C in an inert atmosphere as opposed to the oxyfluoride that should retain its tysonite structure.²⁰ Our nanocomposite retransformed into orthorhombic BiF_3 after such a treatment, suggesting that it is the pure BiF_3 tysonite and not $\text{BiO}_8\text{F}_{3-28}$.

After 1 h of high-energy milling, the ratio of tysonite/orthorhombic phases has been evaluated as 70:30 from the relative intensity of their respective I_{100} Bragg reflections. This ratio increases with milling time, and the transformation is complete after a milling time between 3 and 4 h. SAED has been performed on the BiF_3/C nanocomposite high-energy milled for 1 h, and the electron diffraction patterns are presented in Fig. 2. Many patterns collected could be indexed either as the pure tysonite phase (pattern a) or the pure orthorhombic phase (pattern b). As the area under scrutiny when the SAED is performed is of about $0.25 \mu\text{m}^2$, this result suggests that the phase transformation is pressure-induced upon contact with the milling balls, as opposed to a gradual transformation induced by the already disproved oxygen substitution route. The residual orthorhombic BiF_3 particles may be a result of the initial *o*- BiF_3 material that may have been buffered from direct impact during high-energy milling.

Another feature clearly apparent on the XRD patterns of Fig. 1 is the broadening of the diffraction peaks between the macro- BiF_3 and the BiF_3/C nanocomposite high-energy milled for 1 h. The majority of the broadening is due to the dramatic diminution of the primary crystallite size, but also has a small contribution from the strain induced in the material by the high-energy milling process. Combined Williamson-Hall²¹ and TEM analyses conducted on the BiF_3/C nanocomposite high-energy milled for 1 h have shown that the BiF_3 crystallite size in this material is widely distributed, with an upper distribution limit in the order of 30 nm.^{14,22} The BiF_3 Bragg reflections did not broaden significantly when the high-energy milling time was further increased, indicating that the size of the primary crystallite did not decrease much further.

First lithiation.—The galvanostatic discharge curve and the XRD patterns obtained during in situ XRD conducted on the BiF_3/C nanocomposite high-energy milled for 1 h during the first lithiation down to 2 V vs Li/Li^+ are presented in Fig. 3a and b, respectively. The progressive appearance of the Bi^0 Bragg reflections and disappearance of the BiF_3 Bragg reflections from the XRD patterns when x in " Li_xBiF_3 " increases clearly demonstrate that a conversion reaction is taking place in the BiF_3/C nanocomposite during the lithiation, according to



The Bi^0 Bragg reflections become visible at a very early stage of the lithiation, at an x in " Li_xBiF_3 " smaller than 0.1. The BiF_3 reflections do not exhibit any shift, indicating that the conversion reaction

starts from the very beginning of the lithiation and that there is no concomitant intercalation reaction of the lithium in the metal fluoride, unlike what has been observed in FeF_3 ¹⁰ and TiF_3 .^{9,23} The LiF Bragg reflections cannot be observed on these patterns as they are overlapped by the Bi^0 reflections and because the X-ray scattering factors of Li and F are much smaller than the X-ray scattering factor of Bi. As the intensities in the in situ experiment are low, those

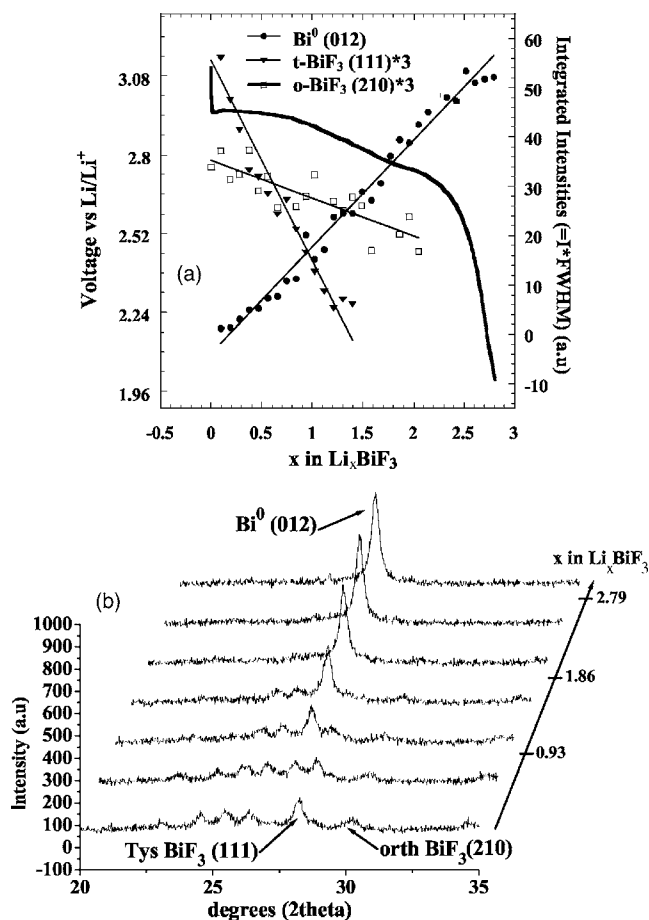


Figure 3. In situ XRD of the *t*- BiF_3/C nanocomposite during the 1st lithiation in a LiPF_6 EC/PC/DEC/DMC electrolyte. The experiment was conducted at room temperature at a current density of 7.58 mAh/g. (a) Galvanostatic curve with integrated intensities of the Bi^0 (012), BiF_3 tysonite (111), and BiF_3 orthorhombic (210) peaks and (b) XRD patterns.

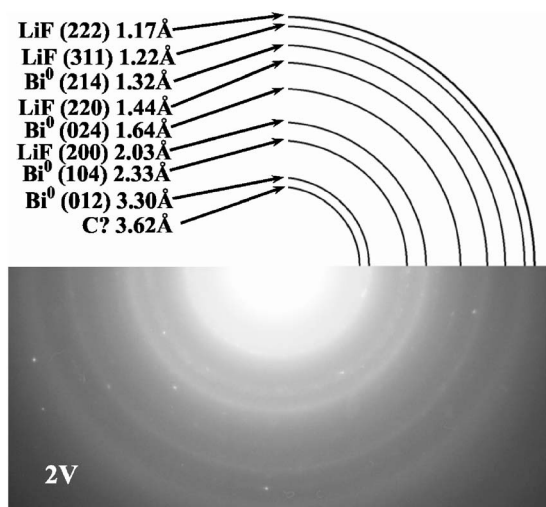


Figure 4. SAED on the BiF_3/C nanocomposite high-energy milled for 1 h and lithiated down to 2 V vs Li/Li^+ at a current density of 7.58 mA/g in a LiPF_6 EC/PC/DEC/DMC electrolyte. It exhibits rings belonging to LiF and Bi^0 . The (015) and (006) Bi^0 rings that partly overlapped the LiF (200) ring, and the (122) Bi^0 ring that partly overlapped the LiF (220) ring, have not been indexed on the figure for the sake of clarity.

peaks cannot be resolved. However, LiF clearly forms during the lithiation and this has been confirmed by SAED as shown on the pattern of Fig. 4 collected on the BiF_3/C nanocomposite lithiated to 2 V. The main LiF rings are, obviously, also overlapped by Bi^0 rings on the SAED pattern of Fig. 4. The overlapping Bi^0 rings are mentioned in the figure caption but have not been indexed on the figure itself for the sake of clarity. In spite of this overlapping issue, the LiF diffraction rings can be clearly observed on this SAED pattern that was collected on an area of the sample where the LiF/ Bi^0 ratio was greater than average and where the diffracting conditions for LiF were particularly well obeyed. A clear distinction between the LiF rings, which appear relatively intense and very diffuse, and the Bi^0 rings, which are less intense and more “spotty,” can thus be made on the SAED pattern presented in Fig. 4. The fact that the (200) and (220) LiF rings on this SAED pattern are very diffuse confirms that the LiF crystallite size is extremely small.

The evolution of the integrated intensities with x of the Bi^0 (012) Bragg reflection, (111) Bragg reflection from the $t\text{-BiF}_3$ phase, and (210) Bragg reflection from the $o\text{-BiF}_3$ phase are overlaid to the galvanostatic curve of Fig. 3a. As the XRD patterns have a poor signal over noise ratio and the peaks are broad, it was quite difficult to accurately fit the patterns for the integrated intensities calculations. The lines added to the figure were obtained by a linear fitting of the integrated intensities data point, but due to the low accuracy of these data points, the fit was not good and those lines should be considered as guides for the eyes only, emphasizing only the general trend. This is also true for all the other in situ XRD figures presented throughout this article.

The integrated intensity of the Bi^0 (012) reflection increases continuously when x increases in Fig. 3a, indicating that the completion of the conversion reaction progresses linearly with x , as expected.

From the evolution of the integrated intensities of the two BiF_3 Bragg reflections it can be inferred that the conversion reaction occurs preferentially in the tysonite phase rather than in the orthorhombic phase. The integrated intensity of the (111) $t\text{-BiF}_3$ peak decreases indeed much faster with x than the integrated intensity of the (210) peak from the $o\text{-BiF}_3$ phase. At an x in “ Li_xBiF_3 ” of about 1.8, only the peaks from the orthorhombic phase can be seen, with integrated intensities similar to their integrated intensities at $x = 0$. We do not know at that point why the conversion reaction occurs preferentially in the $t\text{-BiF}_3$ phase.

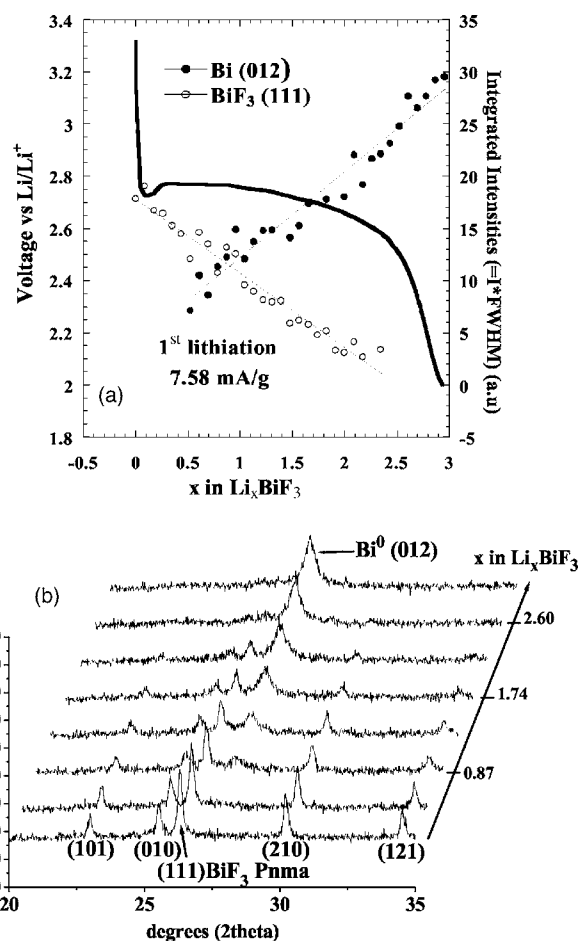


Figure 5. In situ XRD of the $o\text{-BiF}_3/\text{C}$ nanocomposite during the 1st lithiation in a LiPF_6 EC/DMC electrolyte. The experiment was conducted at room temperature at a current density of 7.58 mA/g: (a) galvanostatic curve with integrated intensities of the Bi^0 (012) and BiF_3 orthorhombic (111) peaks and (b) XRD patterns.

Although the conversion reaction takes place preferentially in the $t\text{-BiF}_3$ phase, it is clear that it also occurs in the $o\text{-BiF}_3$ phase. This is demonstrated in Fig. 5 with an in situ XRD experiment conducted on the pure $o\text{-BiF}_3/\text{C}$ nanocomposite. The experiment was conducted in a LiPF_6 EC/DMC electrolyte and the current density was 7.58 mA/g. Figure 5 is divided into two parts: part (a) that describes the variation with x of the output voltage and of the integrated intensities of the Bi^0 (012) and orthorhombic BiF_3 (111) Bragg reflections and part (b) where the in situ XRD patterns are presented. The XRD patterns reveal the progressive increase of the Bi^0 XRD peaks and the progressive decrease of the BiF_3 peaks, as expected from a typical conversion reaction. It is interesting to see that on both Fig. 3 and 5, the $o\text{-BiF}_3$ Bragg reflections remain visible until a much more advanced state of completion of the conversion reaction than the $t\text{-BiF}_3$ reflections do. We know that in both nanocomposites the BiF_3 crystallite size is in the order of 30 nm but that it has a large distribution in the BiF_3/C nanocomposite high-energy milled for 1 h, 30 nm being the upper limit of the distribution, whereas it is more homogeneous in the orthorhombic one.^{14,22} On average, the crystallite size is therefore larger in the $o\text{-BiF}_3/\text{C}$ nanocomposite, and this may explain why the orthorhombic phase remains visible by XRD for a deeper lithiation.

The galvanostatic curve of the first lithiation of the BiF_3/C nanocomposite high-energy milled for 1 h shown in Fig. 3a is divided into two pseudo plateaus at 2.95 and 2.75 V. The occurrence of the first plateau seems to be associated with the $t\text{-BiF}_3$ because the

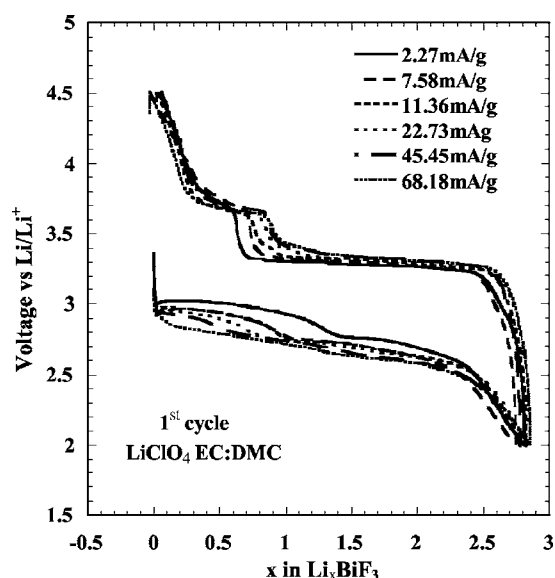


Figure 6. First cycle of the BiF_3/C nanocomposite at different current densities in a LiClO_4 EC/DMC 0.4 M electrolyte.

galvanostatic curve of the pure $o\text{-BiF}_3/\text{C}$ nanocomposite in Fig. 5a only exhibits one single plateau at 2.7 V. However, the same type of division in two plateaus has also been observed in other $\text{BiO}_x\text{F}_{3-2x}/\text{C}$ nanocomposites such as $\text{BiO}_{0.5}\text{F}_2/\text{C}$ during the fluoride conversion.¹³ An identical separation of the two pseudo plateaus also occurs on the voltage profile of the BiF_3/C nanocomposite high-energy milled for 4 h, which has no residual $o\text{-BiF}_3$ phase at all. The separation is more or less severe depending on the electrolyte. It is, for instance, very pronounced in a LiClO_4 EC/DMC electrolyte, as shown in Fig. 6. As it can be seen from the same figure, the voltage on this first plateau is much more rate-sensitive than on the second plateau, thus suggesting that the reaction associated with the plateau is not capacitive or pseudocapacitive in nature. As shown in Fig. 7, when the temperature is increased the voltage on the first plateau increases significantly and at 75°C the separation of the lithiation into two distinct plateaus has been virtually eliminated, with the higher voltage plateau region being the preferred reaction.

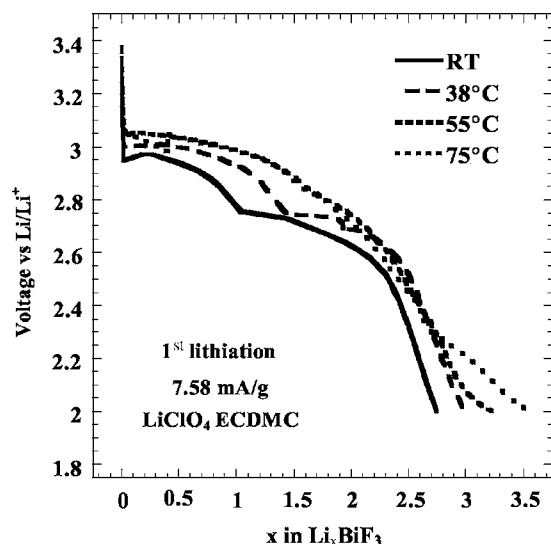


Figure 7. First lithiation of the BiF_3/C nanocomposite at different temperatures in a LiClO_4 EC/DMC 0.4 M electrolyte. The current density was 7.58 mA/g.

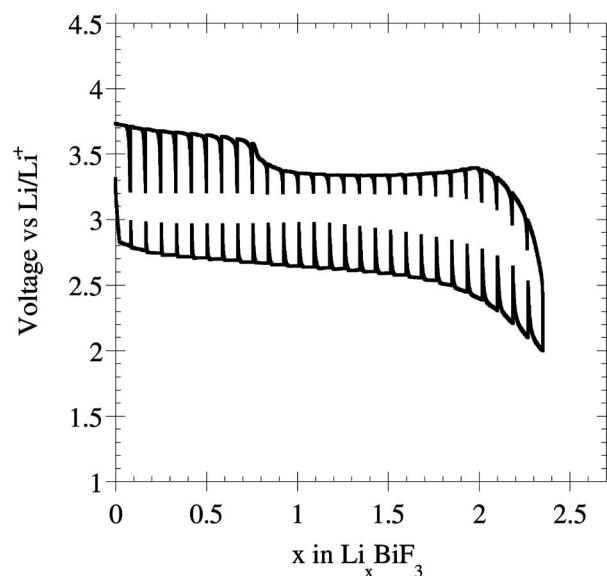


Figure 8. GITT for the first cycle of the $t\text{-BiF}_3/\text{C}$ nanocomposite in a LiPF_6 EC/PC/DEC/DMC electrolyte. The current density was 7.58 mA/g. The current was turned on for 1 h and then stopped for 5 h.

The results of Fig. 6 and 7 suggest that this separation of the lithiation in the two plateaus is a pure kinetics effect. This is confirmed on the galvanostatic intermittent titration technique (GITT) curves of the $t\text{-BiF}_3$ and $o\text{-BiF}_3$ nanocomposites presented in Fig. 8 and 9, respectively. It is clear in these two figures that the lithiation output voltage after relaxation is perfectly flat, as expected from thermodynamics because conversion reactions are two-phase reactions.

If the occurrence of these two plateaus during the lithiation is due to kinetics effects, the kinetics that develop the pseudo plateaus are most likely associated with different electronic and ionic transport mechanisms of the different phases present at the different stages of the lithiation reaction. Considering the dramatic difference in nature of the lithiation reactant (BiF_3) and products ($\text{LiF} + \text{Bi}^0$), this seems a plausible hypothesis. Schematics of the two suggested

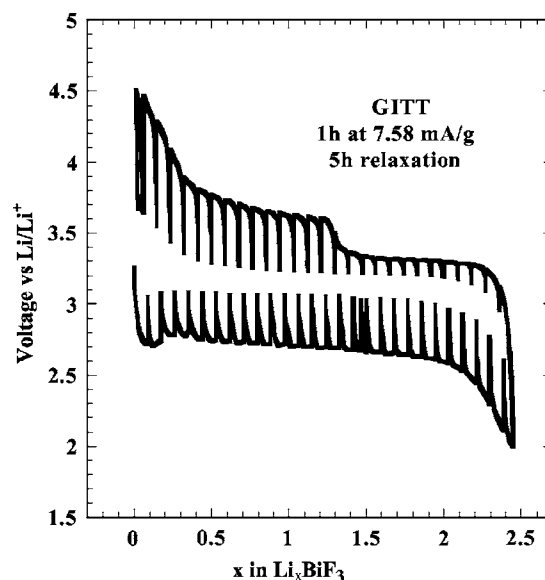


Figure 9. GITT for the first cycle of the $o\text{-BiF}_3/\text{C}$ nanocomposite in a LiPF_6 EC/PC/DEC/DMC electrolyte. The current density was 7.58 mA/g. The current was turned on for 1 h and then stopped for 5 h.

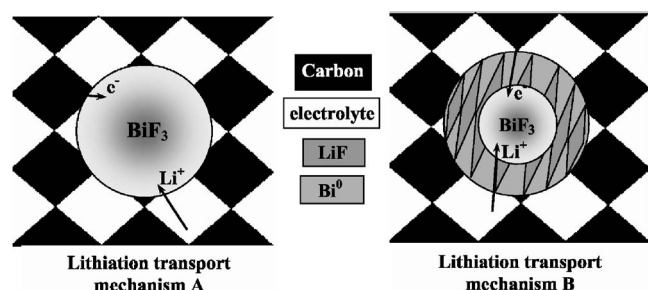


Figure 10. Schematics of the two different transport mechanisms suggested for the lithiation. Mechanism A (x in " Li_xBiF_3 " < 1.5): the electrons are transferred to the BiF_3 surface via the carbon matrix and the Li^+ ions migrate to the BiF_3 surface directly from the electrolyte, inducing the reduction into Bi^0 and LiF . Mechanism B (x in " Li_xBiF_3 " > 1.5): all the surface of the BiF_3 particles has been reduced. To reach the unreacted BiF_3 in the core of the particles the Li^+ ions diffuse through the defect boundaries of the LiF and Bi nanoparticles and the electrons are transferred to BiF_3 via the Bi^0 metal.

lithiation transport mechanisms are provided in Fig. 10. At the beginning of the lithiation the nanocomposite is composed of BiF_3 nanoparticles surrounded by a carbon matrix. Due to the extremely high porosity of the carbon matrix, one can imagine that the metal fluoride particles are also in direct contact with the electrolyte, enabling facile ionic transport. At that early stage of the reaction, the electrons are transferred to the BiF_3 surface via the carbon matrix and that the Li^+ ions migrate to the BiF_3 surface directly from the electrolyte, inducing the surface conversion into Bi^0 and LiF (transport mechanism A in Fig. 10). After a certain degree of completion of the conversion reaction, the entire surface of the BiF_3 particles has reacted. This point is dependent on the specific surface area of the bismuth fluoride. The nanocomposite is then composed of BiF_3 crystallites of only a few nanometers (< 10 nm) surrounded by the conversion reaction products, Bi^0 and LiF , and not by the carbon matrix anymore. At this point the transport mechanisms change dramatically as the Li^+ ion diffusion takes place through the defect boundaries of the LiF and Bi nanocrystallites. Electrons are transferred to the core BiF_3 via the percolation of the metal Bi^0 (transport mechanism B in Fig. 10). Such dramatic difference in transport mechanisms could indeed justify a dramatic polarization change, leading to the occurrence of these two pseudo plateaus during the lithiation.

As can be seen in Fig. 3a, the evolution of the integrated intensities of the BiF_3 Bragg reflections with x nicely supports our hypothesis. As a matter of fact, the x at the end of the first plateau matches relatively well the x value at which the BiF_3 Bragg reflections disappear from the XRD patterns. The same result has been observed in an in situ XRD experiment conducted on the same nanocomposite but in the LiClO_4 EC/DMC electrolyte.¹³ Hence, the inflection point on the galvanostatic curve occurs at a stage of the lithiation when the core BiF_3 particles become of extremely small dimensions, small enough not to be identified by XRD, and are most likely surrounded by the lithiation reaction products. At that point the transport mechanism changes, going from transport mechanism A to transport mechanism B.

The GITT curve of the $t\text{-BiF}_3$ nanocomposite in Fig. 8 indicates that the polarization increases with x , going from about 0.1 V at the beginning of the lithiation when the nanocomposite is constituted of BiF_3 nanoparticles surrounded by the carbon matrix, to about 0.3 V at the end of the lithiation when the nanocomposite is constituted of extremely nano BiF_3 particles surrounded by Bi^0 and LiF particles. The polarization is therefore greater with transport mechanism B than with transport mechanism A.

As can be seen from the GITT curve presented in Fig. 9, the polarization in the $o\text{-BiF}_3/\text{C}$ nanocomposite is, on the other hand, approximately equal to 0.3 V all the way from the beginning to the

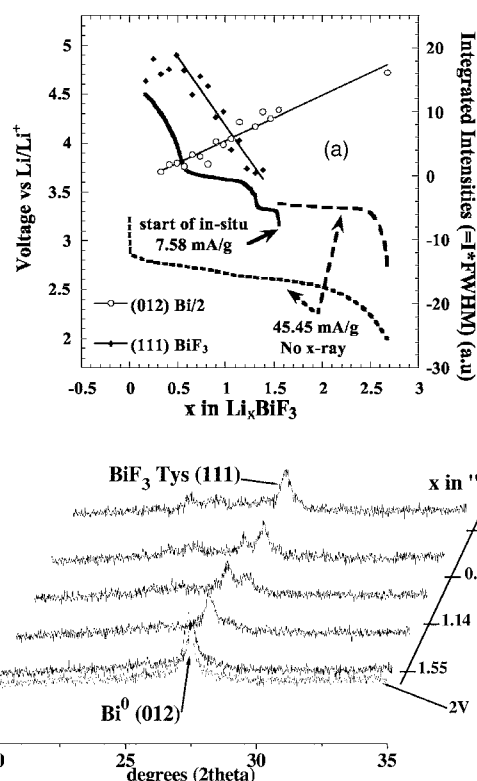


Figure 11. In situ XRD of the $t\text{-BiF}_3/\text{C}$ nanocomposite during the 1st delithiation in a LiPF_6 EC/DMC electrolyte. The nanocomposite was first lithiated in the in situ cell at a current density of 45.45 mA/g without the X-ray. One XRD pattern was collected at the end of the lithiation at 2 V. The nanocomposite was then delithiated until $x \approx 1.55$ in the in situ cell at a current density of 45.45 mA/g without X-ray before the start of the actual in situ XRD. The experiment was conducted at room temperature at a current density of 7.58 mA/g. (a) Galvanostatic curve with integrated intensities of the Bi^0 (012) and BiF_3 tysonite (111) peaks and (b) XRD patterns.

end of the lithiation. This suggests that in this nanocomposite the only transport mechanism that takes place is the transport mechanism B. This is a plausible hypothesis because, as mentioned before, the average crystallite size is greater in the $o\text{-BiF}_3/\text{C}$ nanocomposite than in the $t\text{-BiF}_3/\text{C}$ nanocomposite. As the surface over volume ratio is proportional to $1/r$, it is much smaller in the $o\text{-BiF}_3/\text{C}$ nanocomposite than in the $t\text{-BiF}_3/\text{C}$ nanocomposite. Therefore, the BiF_3 crystallites become covered by LiF and Bi^0 much faster in the lower surface area $o\text{-BiF}_3/\text{C}$ material, hence justifying the occurrence of transport mechanism B. Because the $o\text{-BiF}_3/\text{C}$ nanocomposite has been prepared by an HF solution treatment of the $t\text{-BiF}_3/\text{C}$ nanocomposite, it is also possible that the $o\text{-BiF}_3$ crystallites are covered with a small passivation layer, which could also explain why the overpotential is 0.3 V right from the beginning of the lithiation.

First delithiation.— The galvanostatic curve and the in situ XRD patterns collected on the first delithiation of the $t\text{-BiF}_3/\text{C}$ nanocomposite are presented in Fig. 11a and b, respectively. For this experiment the disk with the active material was first lithiated to 2 V at a current density of 45.45 mA/g in the in situ cell without X-ray analysis. The cycling was stopped at the end of the lithiation and an XRD pattern was collected. The same in situ cell was then restarted on charge, still at a current density of 45.45 mA/g without the X-ray, for a little more than 2 h, at which point the in situ XRD was started. The current density for the in situ XRD analysis was 7.58 mA/g and the electrolyte used was LiPF_6 EC/DMC. The XRD patterns obtained in situ clearly reveal the reformation of $t\text{-BiF}_3$ during delithiation. This experiment therefore proves without any

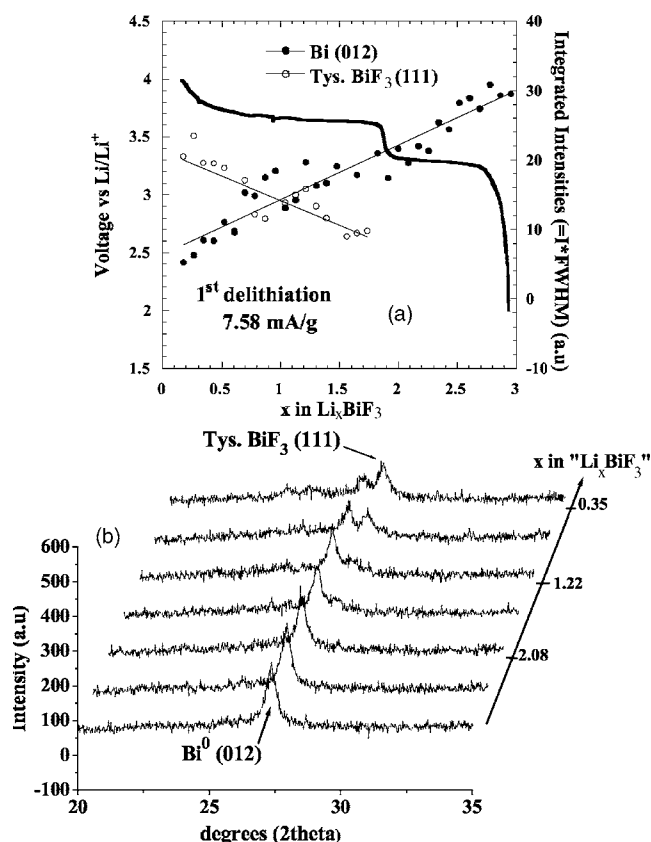
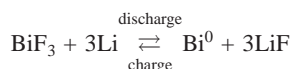


Figure 12. In situ XRD of the *o*-BiF₃/C nanocomposite during the 1st delithiation in a LiPF₆ EC/DMC electrolyte after a 1st lithiation at 2 V. The experiment was conducted at room temperature at a current density of 7.58 mAh/g. (a) Galvanostatic curve with integrated intensities of the Bi⁰ (012) and tysonite BiF₃ (111) peaks and (b) XRD patterns.

possible doubt that the conversion reaction that takes place in the BiF₃/C nanocomposite during the lithiation is reversible. The overall chemical reaction is



Only the tysonite form of BiF₃ is observed at the end of the delithiation on the X-ray data presented in Fig. 11b. As shown by means of in situ XRD of the *o*-BiF₃ in Fig. 12 (collected during the same in situ run as the one from Fig. 5), only the tysonite BiF₃ forms during the delithiation, even when the starting material is the pure *o*-BiF₃/C nanocomposite. This result further demonstrates that the high-pressure polymorph of BiF₃ forms preferentially during the reconversion reaction.

Another striking feature of the in situ XRD patterns of Fig. 11b is that the BiF₃ Bragg reflections begin to be visible only at an advanced state of completion of the delithiation, at an *x* in "Li_{*x*}BiF₃" in the order of 1.3. As can be seen in Fig. 10a, this *x* value matches well the *x* value at which the first delithiation plateau ends and the voltage increases sharply before reaching the second plateau at 3.7 V. The identical result was obtained in the in situ XRD of the *o*-BiF₃/C nanocomposite (cf. Fig. 12) and in the in situ XRD analysis performed on the *t*-BiF₃/C nanocomposite in a LiClO₄ EC/DMC electrolyte.¹³ Hence, based on the XRD results, it would seem that the only bismuth compound present in the nanocomposite along this first plateau is Bi⁰ and that the actual reconversion reaction begins only at the second plateau at higher voltage.

As the first delithiation plateau covers approximately two thirds of the delithiation and the capacity on the second discharge is almost

Table I. Summary of discharge and charge capacities for the Li/BiF₃ cell used for in situ XAS.

Cycle	Current (mA)	Time (h)	Capacity (mAh)
1st discharge	0.20	14.083	2.82
1st charge	0.25	11.639	2.91
2nd discharge	0.25	10.472	2.62
2nd charge	0.25	11.472	2.87

identical to the capacity on the first discharge, there can nevertheless be no doubt that some if not the majority of the reversibility comes from this first plateau. Furthermore, as seen in Fig. 11a and 12a, the integrated intensity of the (012) Bi⁰ Bragg reflection clearly decreases along the first delithiation plateau, indicating that the amount of Bi⁰ in the material decreases continuously along this 3.3-V plateau.

In order to provide a fundamental understanding of the origin of the redox reaction on the first delithiation plateau, XAS was used to monitor the evolution of the electronic and atomic structure of Bi under in situ conditions. The discharge and charge capacities are summarized in Table I. The cell was discharged and charged within the potential range of 2.0–4.5 V vs Li/Li⁺. The X-ray absorption near edge structure (XANES) data, collected during the first cycle of charging, are shown in Fig. 13 as a function of state of charge and vs Bi⁰ and Bi³⁺F₃ standards. The data suggest the direct oxidation of metallic Bi⁰ to Bi³⁺ in BiF₃ during the charging of a discharged BiF₃ cathode. Structurally, this conclusion is also supported by the Fourier transform EXAFS data displayed in Fig. 14, as a function of state of charge, along with those for metallic Bi and BiF₃ as reference standards.

The Fourier transform of EXAFS data for metallic Bi displays a doublet at 2.499 and 3.148 Å, which corresponds to contributions from 3 Bi atoms at the crystallographic distance of 3.073 Å and 3 Bi atoms at 3.527 Å, respectively. The Fourier transform of BiF₃, on the other hand, displays mainly a single peak at 1.549 Å, which corresponds to contributions from 8 F atoms. For the discharged cathode, as expected, the Fourier transform mainly shows the presence of metallic Bi. During charge the Fourier transforms display both the Bi–F and Bi–Bi contributions, the Bi–F contribution in-

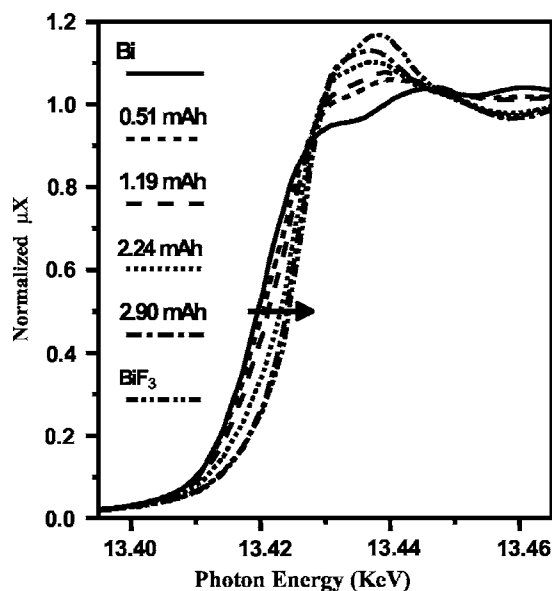


Figure 13. XANES data collected during the 1st cycle of charging a discharged BiF₃ cathode at 0.25 mA (as a function of state of charge). The horizontal arrow indicates the progression of spectra during the charge cycle.

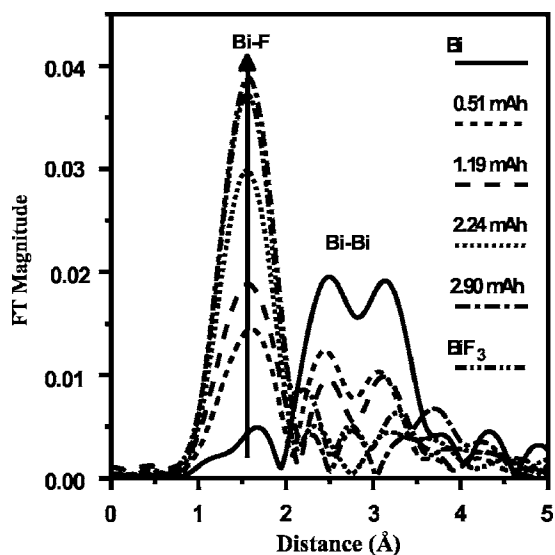


Figure 14. Phase-uncorrected Fourier transforms of k^3 -weighted EXAFS data collected during the 1st cycle of charging a fully discharged BiF_3 cathode at 0.25 mA (as a function of state of charge). The vertical arrow indicates the progression of spectra during the charge cycle. Fourier transform range is 2.85–10.0 Å.

creasing and the Bi–Bi contribution decreasing with the state of charge in a distinct two-phase manner. Finally, the Fourier transform for the charged cathode is consistent with that of BiF_3 .

The in situ XAS study therefore suggests that the reconversion reaction to $t\text{-BiF}_3$ does indeed commence from the beginning of the delithiation. The data also reveal that there is no intermediate bismuth fluoride compound forming in which the oxidation state of the bismuth is lower than 3, which is a rare but distinct and plausible possibility. The presence of reformed tysonite BiF_3 along the first delithiation plateau at lower voltage has also been confirmed by SAED, as shown in Fig. 15. This SAED pattern has been collected on the BiF_3/C nanocomposite delithiated to the end of the first plateau at 3.35 V after a first lithiation down to 2 V. All the diffraction rings on this pattern could be indexed on the basis of the BiF_3

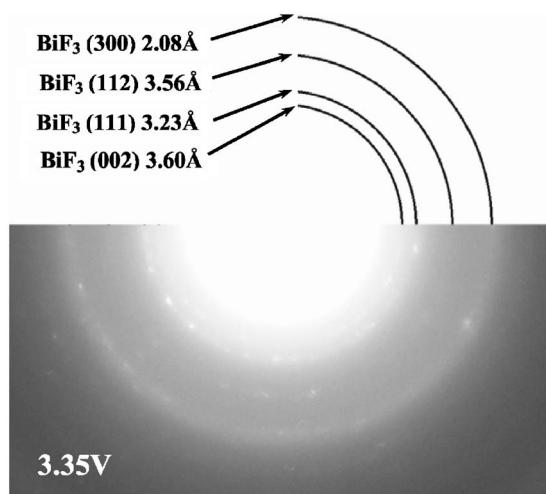


Figure 15. SAED on the BiF_3/C nanocomposite high-energy milled for 1 h and delithiated to 3.35 V vs Li/Li^+ after a 1st lithiation at 2 V. The current density was 7.58 mA/g and the electrolyte LiPF_6 EC/PC/DEC/DMC. The (reconverted) tysonite BiF_3 rings can clearly be identified.

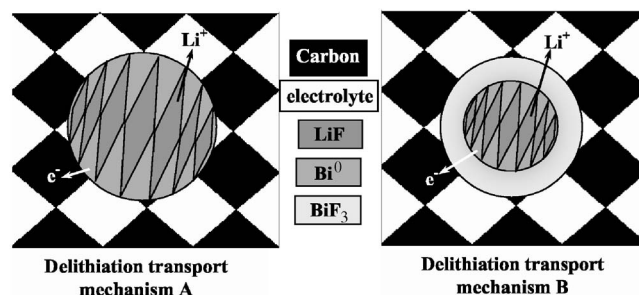


Figure 16. Schematics of the two different transport mechanisms suggested for the delithiation. Mechanism A (x in " Li_xBiF_3 " > 1): the electrons are transferred to the carbon matrix from the Bi^0 nanoparticles near the surface of the $(\text{Bi}^0 + \text{LiF})$ aggregate and the Li^+ ions migrate to electrolyte from the LiF nanoparticles near the surface of the $(\text{Bi}^0 + \text{LiF})$ aggregate, inducing the oxidation of Bi^0 into BiF_3 . Mechanism B (x in " Li_xBiF_3 " < 1): all the surface of the $(\text{Bi}^0 + \text{LiF})$ aggregate has been oxidized into BiF_3 . For the delithiation reaction to proceed the electrons have to tunnel from the remaining Bi^0 nanoparticles to the carbon matrix through the BiF_3 layer and the Li^+ ions have to diffuse from the remaining LiF nanoparticles to the electrolyte through the BiF_3 layer.

tysonite structure. Other SAED, not shown here, obtained on the same sample were characteristic of Bi metal, as expected.

The only possible way to reconcile the in situ XRD data, on which the reconverted BiF_3 can be seen only on the second plateau at higher voltage, and the SAED and in situ XAS data, which shows that BiF_3 does indeed reform on the first plateau as well, is that the primary crystallite size of the reconverted BiF_3 on the first delithiation plateau is too small to be resolved by XRD. Similar to the situation resolved during lithiation, the separation of the delithiation voltage profile in two plateaus at about 3.3 and 3.7 V is a pure kinetics effect and is due to a polarization increase.

A GITT experiment was performed on the BiF_3/C tysonite orthorhombic nanocomposites and the plots shown in Figs. 8 and 9, respectively, support our theory. It is clear that the voltage after relaxation is the same on both delithiation plateaus, indicating that the same reaction (i.e., the BiF_3 reconversion reaction) is taking place on both plateaus as opposed to an alternative phase formation. The same result has obviously been observed on the GITT curve of the $t\text{-BiF}_3/\text{C}$ nanocomposite, because, as mentioned before, only the tysonite form of BiF_3 reforms during the delithiation, the two nanocomposites being therefore essentially identical at the end of the first lithiation. The fact that the sudden voltage increase during the delithiation is related to a polarization increase is further supported by Fig. 6 where the first cycle of the $t\text{-BiF}_3$ nanocomposite at different rate is presented. Hence, when the current density is increased the transition from the 3.3-V plateau to the 3.7-V plateau occurs at an earlier stage of the delithiation, as one would expect for a kinetically limited transition.

Analogous to what we have proposed for the lithiation reaction, the division of the delithiation reaction in two plateaus due to kinetics effects can be understood in terms of transport mechanisms. Schematics of the two proposed transport mechanisms for the delithiation are depicted in Fig. 16. At the end of the lithiation, what were the BiF_3 nanoparticles in the initial nanocomposite are now aggregates of fine Bi^0 and LiF nanoparticles arranged in a shell. When the oxidation reaction commences, the Li^+ ions diffuse from the LiF nanoparticles near the surface of the aggregates directly into the electrolyte and the electrons are transferred from the Bi^0 nanoparticles near the surface of the $(\text{LiF} + \text{Bi}^0)$ aggregates directly to the carbon matrix, inducing the oxidation of the bismuth metal into BiF_3 (transport mechanism A in Fig. 16). The kinetic hindrances for those electronic and ionic transport mechanisms are small, and therefore, the polarization is small (less than 0.1 V according to the GITT plot of Fig. 9), resulting in a plateau at 3.3 V vs Li/Li^+ . After

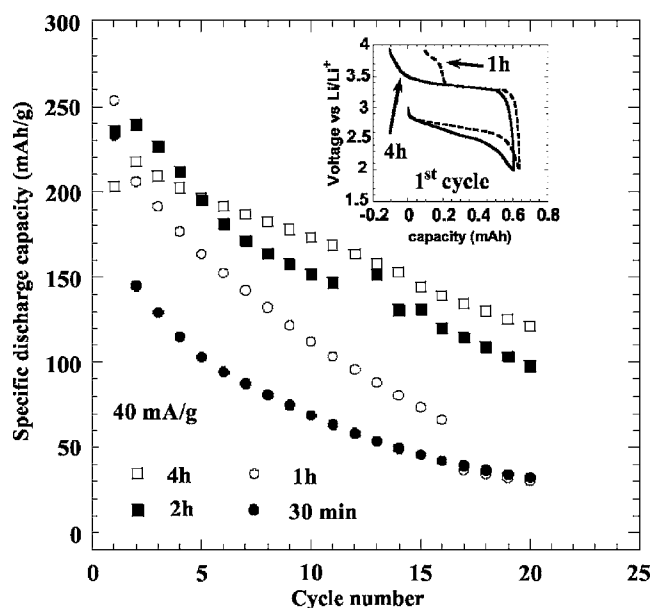


Figure 17. Specific discharge capacities vs cycle numbers for the BiF_3/C nanocomposite high-energy milled for 30 min, 1 h, 2 h, and 4 h. The coin cells were cycled between 2 and 4 V at a current density of 40 mA/g in a LiPF_6 EC/PC/DEC/DMC electrolyte.

a while, the surface has been fully oxidized and all the ($\text{LiF} + \text{Bi}^0$) aggregates are covered with an electron insulative BiF_3 layer. The electronic and ionic transport mechanisms change, going from what we called mechanism A in Fig. 16 to mechanism B. In that proposed transport mechanism, the electrons have to tunnel from the remaining Bi^0 nanoparticles at the core of the aggregates to the carbon matrix through the BiF_3 layer. Likewise the Li^+ have to diffuse through this fluoride layer, migrating from the remaining LiF nanoparticles at the core of the aggregate to the electrolyte. Obviously, the kinetics hindrances are much more severe in mechanism B than they were in mechanism A, and the polarization increases suddenly and significantly (by about 0.3 V according to the GITT curve of Fig. 9), the output voltage then entering the second plateau at 3.7 V. Because this transition is due to the formation of a (proportionally) thick BiF_3 layer on the surface of the ($\text{LiF} + \text{Bi}^0$) aggregates, this also explains why the BiF_3 only became visible by XRD on the second delithiation plateau.

The sudden polarization increase leading to the second plateau occurs at an earlier stage of delithiation in the $o\text{-BiF}_3/\text{C}$ nanocomposite than in the $t\text{-BiF}_3$ nanocomposite, as evident from the comparison of Fig. 11a and 12a. This experimental observation can also be explained with our proposed model. As mentioned earlier, the average BiF_3 crystallite size is larger in the $o\text{-BiF}_3/\text{C}$ nanocomposite than in the $t\text{-BiF}_3$ nanocomposite. This means that the size of the ($\text{LiF} + \text{Bi}^0$) aggregates at the end of the lithiation is also larger in the $o\text{-BiF}_3/\text{C}$ nanocomposite than in the $t\text{-BiF}_3$ nanocomposite, and thus the surface over volume ratio is smaller in the former than in the latter. During the delithiation reaction, the surface of the ($\text{LiF} + \text{Bi}^0$) aggregates therefore become covered by the BiF_3 layer at an earlier stage of the conversion reaction and the polarization increase, brought about by the formation of this layer and the resulting transition from transport mechanism A to transport mechanism B, happens earlier.

The specific discharge capacity vs cycle number plot of the $t\text{-BiF}_3/\text{C}$ nanocomposite high-energy milled for 30 min, 1 h, 2 h, and 4 h and cycled between 2 and 4 V at a current density of 40 mA/g in a LiPF_6 EC/PC/DEC/DMC electrolyte is presented in Fig. 17. It is clear from this figure that the cycling stability, although poor, improves significantly when the milling time is increased. Al-

though from the XRD patterns shown in Fig. 1 the BiF_3 crystallite size does not seem to decrease much when the milling time is increased, the distribution of crystallite size is probably different. Hence, the longer the milling time the more the nanocomposite has BiF_3 crystallites of extremely small dimensions and the less it has 30-nm BiF_3 crystallites. If the average particle size gets smaller when the high-energy milling time is increased, the surface over volume ratio of the BiF_3 particles becomes larger and the transition from transport mechanism A to transport mechanism B during the delithiation occurs later. This would explain why, as can be seen in the inset of Fig. 17, the $t\text{-BiF}_3/\text{C}$ nanocomposite high-energy milled for 4 h does not exhibit the second plateau at 3.7 V during delithiation. The smaller average crystallite size may also justify the improved capacity retention when the milling time is increased.

Conclusion

The reversible conversion reaction occurring in the BiF_3/C nanocomposite when it is cycled against lithium metal has been studied by electrochemical methods, in situ XRD, in situ XAS, and SAED. All the results obtained confirm that BiF_3 is fully reduced to ($\text{Bi}^0 + \text{LiF}$) during lithiation and is fully reformed during the following delithiation.

It has been demonstrated that both lithiation and delithiation reactions are two-phase reactions. No intermediate bismuth fluoride or lithium bismuth fluoride compounds where the oxidation state of the bismuth differs from 0 or 3 have been identified at any stage of the conversion or reconversion reactions.

It has been shown that regardless of the amount of orthorhombic BiF_3 in the initial nanocomposite, only the tysonite form of BiF_3 reforms during delithiation.

Finally, it has been demonstrated that the different voltage plateaus or pseudo plateaus occurring during lithiation and delithiation may stem from kinetic, as opposed to thermodynamic, effects. A model based on the variation of the electronic and ionic transport mechanisms with the composition has been proposed to explain those plateaus.

Acknowledgments

The authors thank J. Gural for his assistance and the United States Government for funding this research. A. N. Mansour acknowledges financial support by the Carderock Division of the Naval Surface Warfare Center's In-house Laboratory Independent Research Program administrated under the Office of Naval Research's Program Element 0601152N.

Rutgers, The State University of New Jersey, assisted in meeting the publication costs of this article.

References

1. R. J. Brodd, K. R. Bullock, R. A. Leising, R. L. Middaugh, J. R. Miller, and E. Takeuchi, *J. Electrochem. Soc.*, **151**, K1 (2004).
2. J. O. Besenhard, *Z. Naturforsch. B*, **33b**, 279 (1978).
3. L. S. Selwyn, W. R. McKinnon, U. von Sacken, and C. A. Jones, *Solid State Ionics*, **22**, 337 (1987).
4. P. Poizot, S. Laruelle, S. Grugeon, L. Dupont, and J.-M. Tarascon, *Nature (London)*, **407**, 496 (2000).
5. P. Poizot, S. Laruelle, S. Grugeon, and J.-M. Tarascon, *J. Electrochem. Soc.*, **149**, A1212 (2002).
6. N. Pereira, M. Balasubramanian, L. Dupont, J. McBreen, L. C. Klein, and G. G. Amatucci, *J. Electrochem. Soc.*, **150**, A1118 (2003).
7. N. Pereira, L. Dupont, J.-M. Tarascon, L. C. Klein, and G. G. Amatucci, *J. Electrochem. Soc.*, **150**, A1273 (2003).
8. S. Grugeon, S. Laruelle, R. Herrera-Urbina, L. Dupont, P. Poizot, and J.-M. Tarascon, *J. Electrochem. Soc.*, **148**, A285 (2001).
9. H. Li, P. Balaya, and J. Maier, *J. Electrochem. Soc.*, **151**, A1878 (2004).
10. F. Badway, N. Pereira, F. Cosandey, and G. G. Amatucci, *J. Electrochem. Soc.*, **150**, A1209 (2003).
11. F. Badway, N. Pereira, F. Cosandey, and G. G. Amatucci, *Mater. Res. Soc. Symp. Proc.*, **756**, 207 (2003).
12. F. Badway, F. Cosandey, N. Pereira, and G. G. Amatucci, *J. Electrochem. Soc.*, **150**, A1318 (2003).
13. M. Bervas, L. C. Klein, and G. G. Amatucci, *J. Electrochem. Soc.*, **153**, A159 (2006).
14. M. Bervas, F. Badway, L. C. Klein, and G. G. Amatucci, *Electrochem. Solid-State Lett.*, **8**, A179 (2005).

15. J. L. Lábár, in *Proceedings of EUREM, 12*, July 2000, Brno, L. Frank and F. Ciampor, Editors, Vol. III, pp. 1379–380 (2000).
16. T. Ressler, *J. Synchrotron Radiat.*, **5**, 118 (1998).
17. T. Ressler, *J. Phys. IV*, **7**, C2–269 (1997).
18. M. Balasubramanian, X. Sun, X. Q. Yang, and J. McBreen, *J. Power Sources*, **92**, 1 (2001).
19. A. Morell, B. Tanguy, and J. Portier, *Bull. Soc. Chim. Fr.*, **7**, 2502 (1971).
20. E. I. Ardashnikova, M. P. Borzenkova, F. V. Kalinchenko, and A. V. Novoselova, *Zh. Neorg. Khim.*, **26**, 1727 (1981).
21. G. K. Williamson and W. H. Hall, *Acta Metall.*, **1**, 22 (1953).
22. M. Bervas, Ph.D. Thesis, *Rutgers, The State University of New Jersey*, Piscataway, NJ (2005).
23. H. Arai, S. Okada, Y. Sakurai, and J. Yamaki, *J. Power Sources*, **68**, 716 (1997).